

Doping-dependent optical properties in YBCO superconducting films via BaHfO3 nanocrystal addition

Shulun Han(韩淑伦), Yuanjie Ning(宁苑杰), Jing Chen(陈静), Yanqun Guo(郭艳群), Zicong Yang(杨子聪), Ping Zhu(朱萍), Zhigang Zeng(曾志刚), Chuanbing Cai(蔡传兵), Xinmao Yin(尹鑫茂), and Lijun Tian(田立君)
Citation: Chin. Phys. B, 2026, 35 (**2**): 027404. DOI: 10.1088/1674-1056/adee87
http://cpb.iphy.ac.cn; http://iopscience.iop.org/cpb

What follows is a list of articles you may be interested in

Large grain size obtained by substrate directly heating for YBCO epitaxial films

Kebin Li(李珂彬), Yifei Zhang(张一飞), Tong Zhang(张同), Shuguang Yi(易曙光), Shi-Peng Zhang(张世鹏), Quan-Ming Gao(高全明), and Shan-Dong Li(李山东)
Chin. Phys. B, 2025, 34 (**9**): 097403. DOI: 10.1088/1674-1056/add4fc

Superconductivity in YbN4H12 under low pressures

Xiang Wang(汪翔), Chenlong Xie(谢晨龙), Haohao Hong(洪浩豪), Yanliang Wei(魏衍亮), Zhao Liu(刘召), and Tian Cui(崔田)
Chin. Phys. B, 2025, 34 (**8**): 087401. DOI: 10.1088/1674-1056/add908

Spin fluctuations and orbital-selective superconductivity in Ba2CuO4-y: A FLEX study

Pei-Jun Zheng(郑裴俊), Ya-Min Quan(全亚民), and Liang-Jian Zou(邹良剑)
Chin. Phys. B, 2024, 33 (**12**): 127401. DOI: 10.1088/1674-1056/ad8cbe

Superconductivity in octagraphene

Jun Li(李军) and Dao-Xin Yao(姚道新)
Chin. Phys. B, 2022, 31 (**1**): 017403. DOI: 10.1088/1674-1056/ac40fa

Enhancing superconductivity of ultrathin YBa2Cu3O7-δ films by capping non-superconducting oxides

Hai Bo(薄海), Tianshuang Ren(任天爽), Zheng Chen(陈峥), Meng Zhang(张蒙), Yanwu Xie(谢燕武)
Chin. Phys. B, 2019, 28 (**6**): 067402. DOI: 10.1088/1674-1056/28/6/067402

Doping-dependent optical properties in YBCO superconducting films via $BaHfO_3$ nanocrystal addition

Shulun Han(韩淑伦)[†], Yuanjie Ning(宁苑杰)[†], Jing Chen(陈静), Yanqun Guo(郭艳群)[‡], Zicong Yang(杨子聪), Ping Zhu(朱萍), Zhigang Zeng(曾志刚), Chuanbing Cai(蔡传兵), Xinmao Yin(尹鑫茂)[§], and Lijun Tian(田立君)[¶]

Shanghai Key Laboratory of High Temperature Superconductors, Department of Physics, Shanghai University, Shanghai 200444, *China*

(Received 11 March 2025; revised manuscript received 10 June 2025; accepted manuscript online 11 July 2025)

This study investigates the effect of $BaHfO_3$ (BHO) addition on the optical properties of $YBa_2Cu_3O_{7-\delta}$ (YBCO) superconducting thin films using spectroscopic ellipsometry. Through Raman spectroscopy and SEM analysis, optimal 10-min Ar ion etching effectively removes surface *a*-axis-oriented grains and Ba–Cu–O impurities, enhancing surface quality. Optical conductivity analysis reveals a doping-dependent evolution: 10% BHO doping maximizes free carrier density and interband transition efficiency, attributed to optimized Cu–O bond contraction and reduced lattice distortions. Higher doping induces defect clustering, carrier scattering, and redshifted transitions due to lattice expansion. Dielectric function and loss function analyses confirm enhanced plasmonic behavior and flux pinning at 10% doping, while excessive doping degrades electronic transitions. These results highlight the critical role of controlled BHO addition and surface treatment in tailoring the optical and superconducting properties of YBCO, offering insights into the interplay among doping, carrier dynamics, and electronic structure in high-temperature superconductors (HTS).

Keywords: high-temperature superconductivity, YBCO films, optical conductivity, spectroscopic ellipsometry

PACS: 74.72.–h, 74.25.Gz, 68.37.–d, 78.20.–e

DOI: 10.1088/1674-1056/adee87 **CSTR:** 32038.14.CPB.adee87

1. Introduction

Oxide high-temperature superconductors (HTS), due to their unique physical properties and promising applications, hold tremendous potential for driving economic and societal advancements in transportation, military, and medical fields.[1–3] Second-generation HTS tapes, REBa$_2$Cu$_3$O$_{7-\delta}$ (REBCO, $RE = Y$ and rare earth), exhibit excellent superconducting properties, including high critical current density, strong irreversibility field at liquid nitrogen temperature (77 K), and robust mechanical performance, making them highly suitable for applications in high fields and large current transmission.[4–7] However, the motion of magnetic flux lines under an electric field in REBCO films causes energy dissipation and a rapid drop in critical current under high magnetic fields,[8,9] thereby limiting their practical efficiency and stability.

Recent advancements in metal–organic deposition (MOD)-processed YBCO films have enabled the incorporation of nanoscale pinning centers to enhance flux pinning.[10] The precise control over the size and distribution of nanoparticles embedded in the films, such as prefabricated nanocrystals of $BaZrO_3$ (BZO) or $BaHfO_3$ (BHO), significantly improves the in-field performance of REBCO nanocomposite films.[11–13] Despite these advancements, systematic investigations into its impact on optical properties, which are closely linked to the microscopic mechanisms of superconductivity, remain both limited and challenging. Therefore, investigating the effects of nanocrystal addition on the optical performance of REBCO films is critical for understanding the carrier dynamics, plasma behavior, and optical responses of superconducting materials.

Spectroscopic ellipsometry (SE) stands out as an exceptionally powerful tool due to its non-destructive nature, high sensitivity, and ability to accurately characterize the optical properties of materials across a broad spectral range.[14–16] It provides valuable insights into how doping influences the electronic states and subtle modifications within the material, offering both experimental and theoretical support for the design and optimization of HTS. In this study, we first employed ion etching to remove impurity phases on the thin film surface, which was verified by Raman spectroscopy and scanning electron microscopy. Subsequently, optical conductivity spectra σ_1 were obtained using SE, revealing how BHO nanocrystal addition (5%, 10%, and 15%) modulates charge transfer transitions and interband excitations in the Cu–O plane. The Drude–Lorentz model provided a detailed interpretation of the doping-dependent trends in carrier density, structural defects,

[†]These authors contributed equally to this work.
[‡]Corresponding author. E-mail: yqguo@shu.edu.cn
[§]Corresponding author. E-mail: yinxinmao@shu.edu.cn
[¶]Corresponding author. E-mail: tianlijun@shu.edu.cn

© 2026 Chinese Physical Society and IOP Publishing Ltd. All rights, including for text and data mining, AI training, and similar technologies, are reserved.

and electronic transitions. Analysis of the dielectric function, $\varepsilon(\omega) = \varepsilon_1(\omega) + \mathrm{i}\varepsilon_2(\omega)$, and the energy loss function further elucidated the correlation between plasmonic behavior and flux pinning effects.

Key findings suggest that at a doping level of 10%, the optical conductivity peak is enhanced due to Cu–O bond contraction and strengthened interband transitions, whereas higher doping (15%) leads to defect clustering and suppressed carrier mobility. This study establishes a critical balance between doping concentration and surface treatment, providing a roadmap for optimizing the optical and superconducting properties of YBCO films. By correlating the evolution of microscopic electronic structures with optical properties, our work advances the rational design of high-performance coated conductors for optical and energy applications and deepens our understanding of how nanocrystals influence the properties of high-temperature superconducting films.

2. Experimental methods

2.1. Sample preparation

BHO nanocrystals were synthesized by polyol solvothermal method in a mixed alcohol solvent of triethylene glycol (TEG) and ethanol (EtOH), following procedures similar to that reported in previous work.[13] The YBCO precursor solution was prepared via a low-fluorine metal–organic deposition (LF-MOD) route. Uniform and monodisperse BHO nanocrystals in ethanol were directly introduced into the LF YBCO precursor solutions at concentrations of 5 mol%, 10 mol%, and 15 mol% relative to Y. The BHO-added YBCO films on the substrate of $LaMnO_3/MgO/Y_2O_3/Al_2O_3$/Hastelloy were fabricated by continuous industrial reel-to-reel systems from Shanghai Creative Superconductor Technologies Co. Ltd. (SCSC),[17] including film coating, pyrolysis, and high-temperature film growth.

2.2. Characterization equipment

The BHO-added YBCO films were etched for 5 min, 10 min, 15 min, 20 min, and 30 min using an IBE-100 ion beam etching machine, with the ions incident perpendicular to the sample surface. The working gas was argon gas, and the etching power was set to 100 W. The x-ray diffraction (XRD) was performed using a SmartLab XRD instrument to analyze the phase structure of the films. Confocal micro-Raman spectroscopy was employed to characterize the phase composition of the samples after different etching durations. Scanning electron microscopy (SEM), conducted with a Hitachi SU 5000 instrument, was used to examine the surface morphology of the films.

2.3. Spectroscopic ellipsometry measurements

Optical characterization measurements were conducted using the RC2 spectroscopic ellipsometer of Woollam Co., Inc. with the photon energy of 0.5 eV–6.0 eV. The ellipsometry parameters Ψ and Δ of the YBCO samples were measured at incident angles 70°. The complex dielectric function $\varepsilon(\omega) = \varepsilon_1(\omega) + \mathrm{i}\varepsilon_2(\omega)$ was also obtained from ellipsometry Ψ and Δ. The ε_2 spectra was further converted to optical conductivity σ_1, based on the equation $\sigma_1(\omega) = \omega\varepsilon_0\varepsilon_2(\omega)$, where ε_0 denotes the permittivity of free space. The $\varepsilon(\omega)$ of YBCO films can be fitted with Drude–Lorentz oscillators according to

$$\varepsilon(\omega) = \varepsilon_0 + \sum_k \frac{\omega_{\mathrm{p},k}}{\omega_{0,k}^2 - \omega^2 - \mathrm{i}\Gamma_k\omega},$$

where ε_∞ is the high frequency dielectric constant; $\omega_{\mathrm{p},k}$, $\omega_{0,k}$, and Γ_k are the plasma frequency, the transverse frequency (eigen frequency), and the line width (scattering rate) of the k-th oscillator, respectively.

3. Results and discussion

3.1. Structural characterization and surface optimization

As shown in Fig. 1(a), the x-ray diffraction (XRD) patterns of the grown YBCO thin films exhibit sharp and well-defined peaks, confirming a strong c-axis preferential orientation. Elemental mapping via energy-dispersive spectroscopy (EDS), presented in Figs. 1(b)–1(e), reveals a uniform elemental distribution and a dense microstructure, further demonstrating the excellent surface quality of the films. Figure 1(f) displays the normalized critical current density (J_C/J_{C0}) for samples with different doping levels, clearly indicating that the incorporation of BHO effectively improves in-field performance. Nevertheless, since J_C primarily reflects macroscopic superconducting behavior, it offers limited insight into the underlying microscopic structural and electronic modulations. As schematically illustrated in Fig. 1(g), the BHO-added YBCO superconducting thin film exhibits uniformly distributed spherical nanocrystalline pinning centers, which significantly enhance its flux pinning capability. To further uncover the underlying mechanisms, particularly the evolution of the electronic structure and carrier dynamics, optical techniques serve as a powerful and complementary probe that enables a deeper understanding of doping-induced modifications.

Notably, due to the unique growth mechanism of the YBCO thin film fabricated via the MOD method, a heterogeneous surface layer composed of Ba–Cu–O impurity phases and a-axis-oriented YBCO grains tends to form after high-temperature crystallization.[18,19] This impurity layer adversely affects light transmission, introducing inaccuracies in optical measurements. To address this issue, Ar ion etching was systematically applied to the surface of the YBCO films prior to the SE experiments. This treatment effectively removed surface impurities without altering the chemical composition or their lattice structure,[20–22] thereby enhancing surface quality and ensuring more reliable measurements.

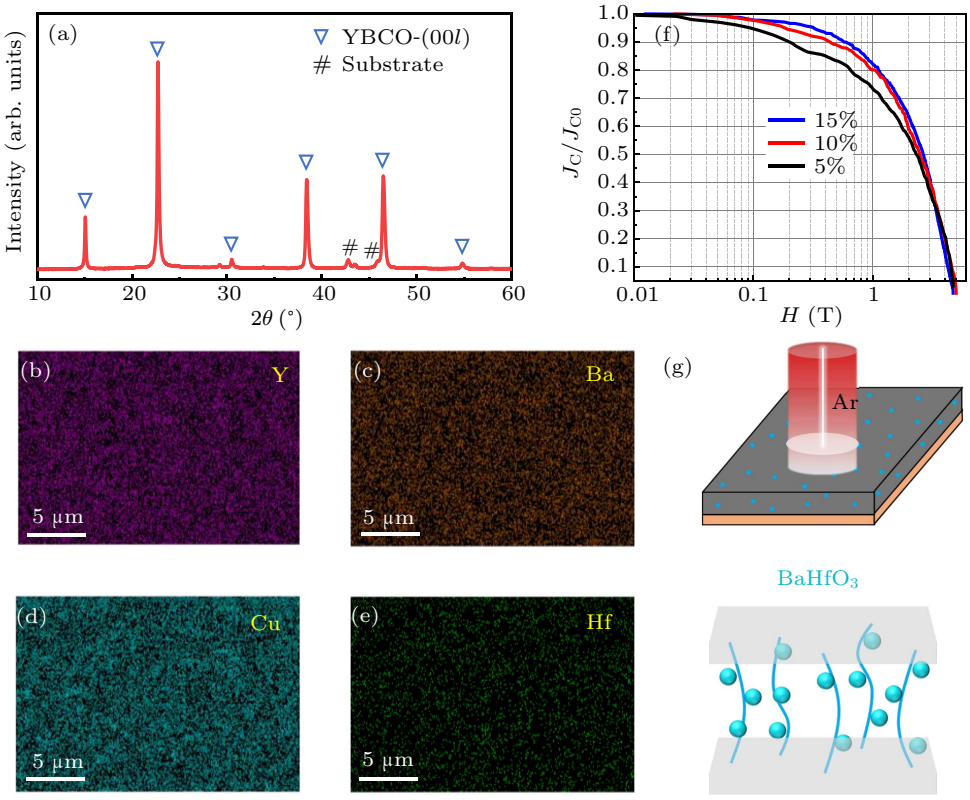


Fig. 1. (a) XRD patterns of the films, demonstrating *c*-axis preferential orientation. (b)–(e) EDS elemental mappings of Y, Ba, Cu, and Hf, respectively, illustrating the distribution of each element within the film. (f) Field dependence of normalized critical current density (J_C/J_{C0}). (g) Schematic illustration of the etching process for BHO-added YBCO films.

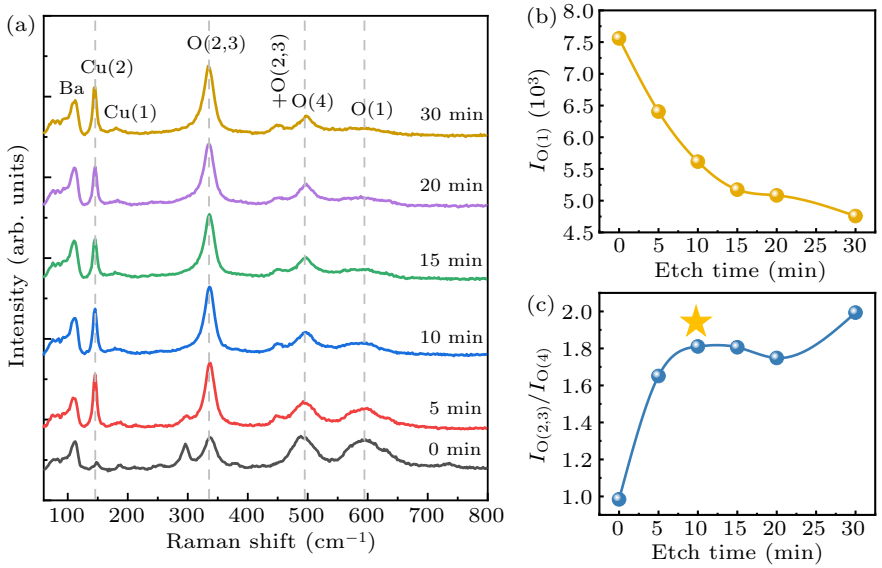


Fig. 2. (a) Raman spectra of BHO-added YBCO films etched for 5 min–30 min. (b) Variation of vibration intensity $I_{O(1)}$ as a function of etching time. (c) Evolution of the intensity ratio $I_{O(2,3)}/I_{O(4)}$ with etching time.

For systematic characterization, 12-mm-wide superconducting tapes were cut into 10-mm-long specimens for etching treatments and subsequent analyses. Raman spectroscopy was employed to characterize the phase composition of YBCO film surfaces and clarify the effects of Ar ion etching at different durations. Figure 2(a) compares the Raman spectra of samples etched for 5 min–30 min with an unetched reference. Seven characteristic Raman bands were identified at approximately 112, 146, 184, 336, 450, 495, and 595 cm^{-1}. Specifically, the peaks at approximately 495 cm^{-1} [O(4) mode] and 595 cm^{-1} [O(1) mode] correspond to the *a*-axis-oriented YBCO grains and Ba–Cu–O heterogeneous phases, respectively.[21,23,24] The prominent O(1) and O(4) modes in the unetched sample confirm that the surface of the MOD-processed films contains a significant amount of *a*-axis-oriented YBCO grains and impurity phases of poor growth quality. As shown in Fig. 2(b), the intensity of the O(1) mode decreases progressively with etching time, indicating an effec-

tive reduction in the impurity layer on the surface. This reduction slows down after 15 min of etching. Additionally, the O(2,3) mode at ~ 336 cm^{-1} represents the vibrational mode of O(2) and O(3) atoms in the Cu–O plane, with higher intensity reflecting improved *c*-axis-oriented growth quality. In contrast, the O(4) mode is closely associated with the *a*-axis-oriented growth of YBCO films. Therefore, the intensity ratio $I_{O(2,3)}/I_{O(4)}$ can serve as a parameter to characterize the film texture; a larger ratio indicates a greater proportion of *c*-axis-oriented grains. Figure 2(c) shows that the ratio increases with etching time and reaches a maximum at 10 min. This suggests that Ar ion etching effectively removes *a*-axis grains and impurity phases from the surface, allowing *c*-axis-oriented YBCO grains to dominate.

To complement the Raman analysis, surface morphology was investigated by scanning electron microscopy (SEM, Hitachi SU 5000). Figure 3 presents the images of the pristine sample and those etched for 5 min, 10 min, and 15 min. In the unetched sample [Fig. 3(a)], micron-sized Ba–Cu–O heterogeneous phase particles are distinctly observed, which could distort optical signals. After 5-min etching [Fig. 3(b)], the number of large impurity particles is substantially reduced, signaling initial surface homogenization. With extended etching to 10 min [Fig. 3(c)], surface impurities are significantly reduced, large particles almost disappear, and interconnected *c*-axis-oriented YBCO domains begin to emerge.

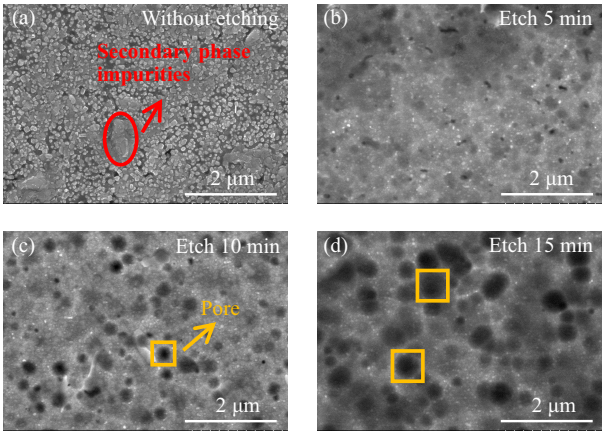


Fig. 3. (a)–(d) SEM images of BHO-added YBCO films before etching and after etching for 5 min, 10 min, and 15 min, respectively, showing the surface morphology evolution.

However, as shown in Figs. 3(b)–3(d), extending the etching duration introduces pore-like features on the sample surface. Notably, after 15-min etching, large pores appear on the surface, primarily due to structural defects caused by prolonged Ar ion bombardment. Such defects may degrade the current-carrying capability of the YBCO films.[25,26] SEM analysis, corroborated by XRD and Raman spectroscopy, confirms that a 10 min Ar ion etching provides the optimal treatment time. This duration is sufficient to eliminate surface contaminants while maintaining the crystalline structure and smooth morphology of the YBCO films, ensuring the integrity of subsequent optical measurements. Based on these findings, we performed etching treatments on YBCO samples with varying BHO concentrations (5%, 10%, and 15%) for subsequent analysis.

3.2. Optical conductivity and doping dependence

In order to analyze the alterations in the optical properties of the BHO-doped YBCO system, optical conductivity, σ_1, was determined from the SE measurements. Figure 4(a) presents the doping-dependent characteristics of films at room temperature. The results reveal a pronounced wavelike rising trend in the σ_1 spectra above 1.5 eV. Compared to previous studies,[27,28] the more prominent peak features observed in our spectra may originate from the high crystalline quality of the thin films, uniform doping distribution, and the precise experimental measurements. Additionally, the micro-stress or local lattice distortions induced by BHO doping[29] significantly affect the energy and intensity distribution of interband transitions. Below 1.5 eV, the optical conductivity increases sharply, exhibiting a Drude-like response, indicating a significant increase in free carrier concentration. The low-energy region is dominated by free carriers, whereas the high-energy region is governed by charge transfer (CT) transitions. With increasing doping concentration, the overall intensity of σ_1 exhibits an initial enhancement followed by a decline. Notably, at lower doping levels (5% and 10%), the peak position remains relatively stable; however, at a higher doping concentration of 15%, a significant red shift is observed. The characteristic peaks at 2.5 eV and 5.5 eV (yellow-shaded regions) undergo particularly significant variations.

To further elucidate the evolution of these two peaks, we employed the Drude–Lorentz model to fit the optical conductivity spectra and extracted the doping-dependent trends of features, which are labeled as peak B and peak G in Fig. 4(b). According to previous studies, peak B can be attributed to the charge transfer transition between Cu 3d and O 2p orbitals. This transition feature is universally present in all copper-oxide superconductors,[30] highlighting its intrinsic nature in the CuO_2 plane. Peak G, on the other hand, corresponds to the interband transition from O 2p states to higher-energy Cu 4s states. The energy positions and intensities of these two peaks are strongly influenced by the local coordination environment of the Cu–O plane.

Figures 4(c) and 4(d) illustrate in detail how the peak intensity and energy positions of peaks B and G vary with doping concentration. In the low-doping regime, the free carrier concentration exhibits a gradual increase, while the structural integrity of the Cu–O planes remains relatively stable, with minimal variations in Cu–O bond lengths and lattice distortions. This dual optimization facilitates a high interband transition efficiency. Notably, BHO addition induces a contraction

of the Cu–O bond length, which elevates the energy level of the Cu 3d orbital,[31,32] thereby enhancing the intensity of the B-peak transitions. Simultaneously, doping-induced modifications to the in-plane local coordination environment significantly perturb the Cu 4s energy level, leading to pronounced variations in the G-peak intensity. Consequently, the B- and G-peak intensities increase markedly with rising doping concentrations from 5% to 10%, as illustrated in Fig. 4(c).

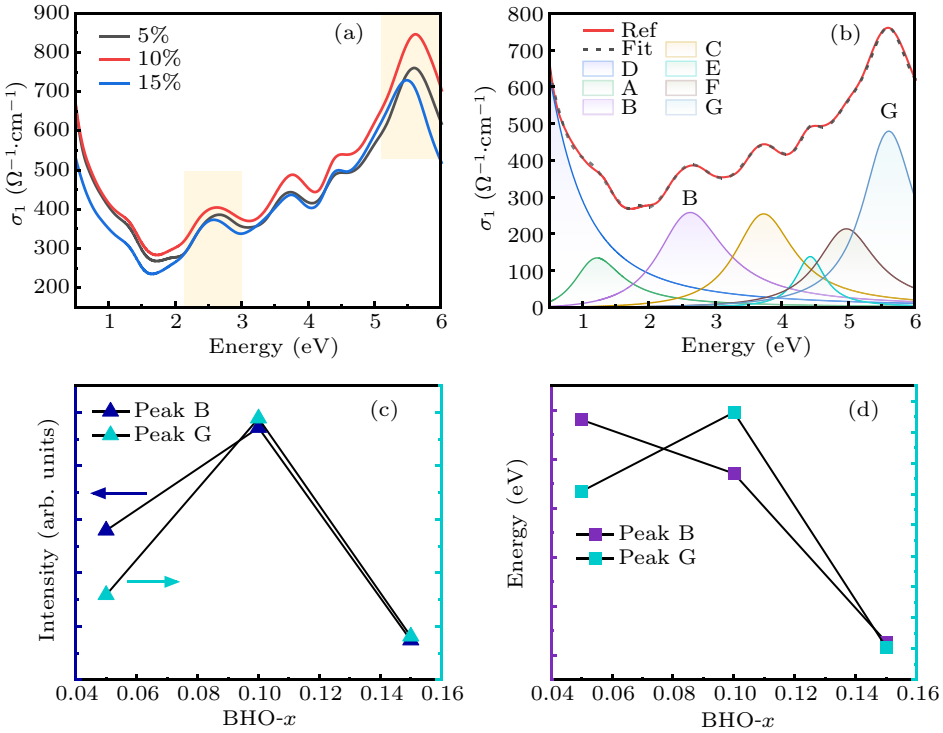


Fig. 4. Doping-dependent optical conductivity and interband transitions in BHO-added YBCO thin films. (a) Optical conductivity (σ_1) spectra at room temperature, showing distinct doping-induced modifications. (b) Drude–Lorentz model fitting of σ_1. (c)–(d) Doping-dependent variations in the intensity and energy positions of peaks B and G.

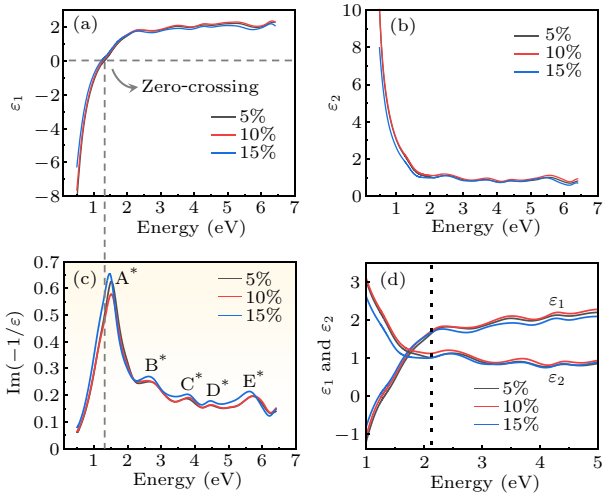


Fig. 5. Dielectric function and energy loss function analysis of BHO-added YBCO thin films. (a)–(b) Real (ε_1) and imaginary (ε_2) components of the dielectric function at different doping concentrations. (c) Energy loss function Im($-1/\varepsilon$), highlighting plasma resonance energy and carrier dynamics. (d) Magnified view of ε_1 and ε_2.

Upon reaching a moderate doping concentration (∼10%), the free carrier concentration and interband transition efficiency attain their maximum values, coinciding with the saturation of both B- and G-peak intensities. However, further increases in doping concentration beyond this threshold amplify carrier scattering effects, suppress carrier mobility, and diminish the contribution of free carriers, ultimately resulting in a progressive reduction of B- and G-peak intensities at 15% doping concentration. At the same time, higher doping concentrations exacerbate local lattice distortions in the CuO_2 plane. These distortions may reconstruct the electronic density of states (DOS) near the Fermi level and alter the symmetry of the Cu–O bonds, thereby contributing to the significant redshift observed at 15% doping, as shown in Fig. 4(d).

3.3. Dielectric function and energy loss analysis

To gain deeper insights, we analyzed the dielectric function, $\varepsilon(\omega) = \varepsilon_1(\omega) + i\varepsilon_2(\omega)$, where ω represents the photon angular frequency, along with its corresponding loss function

$$\mathrm{LF} = \mathrm{Im}\left(\frac{1}{\varepsilon(\omega)}\right) = \frac{\varepsilon_2(\omega)}{\varepsilon_1^2(\omega) + \varepsilon_2^2(\omega)}.$$

This set of analyses is essential for providing additional insights into the plasmonic behavior of BHO-added YBCO films and its evolution with varying doping concentrations.

Figures 5(a) and 5(b) demonstrate that the dielectric functions (real part ε_1 and imaginary part ε_2) of YBCO thin films at different doping concentrations exhibit similar optical responses, suggesting that the overall electronic structures of the samples remain largely consistent, which in turn minimizes their impact on the superconducting transition temperature (T_C).[11] Experimentally, as the frequency decreases, ε_1

gradually decreases, crosses zero near $\hbar\omega = 1.3$ eV, and then drops further into negative values, as shown in Fig. 5(a). The plasma frequency ω_p, corresponding to the zero-crossing point of ε_1,[27] aligns well with reported values for high-quality YBCO samples. Meanwhile, as shown in Fig. 5(b), ε_2 increases significantly from approximately 1, exhibiting typical Drude-like behavior that reflects a strong carrier response in the low-energy region.

With increasing doping concentration, figure 5(d) reveals a clear crossover around 2.2 eV, demarcating the carrier-dominated low-frequency behavior from the Cu–O interband transition-dominated high-frequency behavior.[32] Notably, the plasma frequency in ε_1 exhibits a slight redshift with increasing doping concentration, primarily due to a marginal decrease in carrier density caused by lattice expansion. In the high-energy region (2 eV–6 eV), the dielectric function of YBCO thin films presents prominent peak structures, with the optical response of the 10% BHO-added sample significantly surpassing that of the others, indicating higher efficiency in high-energy interband transitions and carrier transport. In contrast, the 15% doping concentration may introduce lattice defects and increase scattering centers, suppressing electronic transitions between high-energy states. This trend is consistent with the observed changes in optical conductivity.

As shown in Fig. 1(f), the J_C/J_{C0} curves at 30 K indicate that the sample doped with 10% BHO exhibits the most stable and gradual decline across the entire magnetic field range, reflecting the strongest flux pinning performance at this concentration. Notably, as the doping level increases further, the enhancement in flux pinning provided by BHO tends to saturate. In the high-field region, the J_C of the 15% doped sample decreases more rapidly than that of the 10% sample, suggesting that excessive doping introduces additional defects or disrupts matrix continuity, ultimately degrading high-field performance. This trend is consistent with our optical observations, reinforcing the conclusion that 10% represents the optimal doping concentration.

The corresponding energy loss function, $\mathrm{Im}(-1/\varepsilon)$, is shown in Fig. 5(c). It exhibits a distinct main peak A* corresponding to the plasma resonance energy, reflecting the collective excitation modes of free carriers in the material, which are closely related to charge transport properties of YBCO superconductors. In all samples, the plasma resonance energy is around 1.5 eV, slightly above the zero-crossing point of ε_1. This disparity arises from the onset of free-electron scattering within the system.[33] With increasing doping concentration, the intensity of the main peak in the energy loss function exhibits a non-monotonic trend, initially decreasing and then increasing, with a notable redshift observed at 15% doping. These results suggest that the 5%-added sample contains fewer defects and relatively weaker scattering effects, resulting in a sharper plasma resonance. At 10% doping, the local stress field is optimized and flux pinning effects are significantly enhanced. However, the peak intensity slightly decreases, which may be attributed to local electronic disorder. At 15% doping, defect clustering or inhomogeneous distribution may lead to increased scattering effects, resulting in a broadened peak. Meanwhile, the peak intensity appears to recover, suggesting that the reconstruction of localized electronic states may enhance specific pinning centers. Additionally, significant changes in peak intensity and full-width at half-maximum are observed at 2.5 eV and 5.5 eV, further indicating that electronic transitions in these energy regions are strongly affected by doping concentration.

4. Conclusion and perspectives

In summary, our study demonstrates that BHO doping significantly influences the optical and electronic properties of YBCO films. Optical conductivity measurements reveal doping-induced modifications in both charge transfer processes and interband transitions. At a moderate doping level (10%), the peak intensity is maximized, coinciding with the highest free carrier concentration, the largest number of transition electrons, and the most efficient interband transitions. Dielectric function and loss function analyses further confirm the significant influence of doping on carrier dynamics, plasmonic behavior, and lattice distortions. The observed redshift in plasma frequency indicates lattice expansion, which affects free carrier density. While optimal doping improves interband transitions and flux pinning effects, excessive doping leads to defect clustering, increased scattering, and suppressed high-energy transitions. Our optical analysis provides valuable insights into the underlying doping mechanisms and their correlation with the electronic and superconducting behavior of the material. These findings not only lay a theoretical foundation for optimizing the functionality of advanced coated conductors but also open new avenues for the rational design of superconducting optoelectronic devices such as terahertz emitters, broadband detectors, and infrared sensors.

Acknowledgements

Project supported by the National Natural Science Foundation of China (Grant Nos. 52172271, 12374378, 52307026, and 52477022), the National Key Research and Development Program of China (Grant No. 2022YFE03150200), and Shanghai Science and Technology Innovation Program (Grant No. 23511101600).

References

[1] Obradors X, Puig T, Pomar A, *et al.* 2006 *Supercond. Sci. Technol.* **19** S13

[2] Yazdani-Asrami M, Seyyedbarzegar S, Sadeghi A, De Sousa W T B and Kottonau D 2022 *Supercond. Sci. Technol.* **35** 083002

[3] Zhou Y H, Park D and Iwasa Y 2023 *Natl. Sci. Rev.* **10** nwad001

[4] Jha A K and Matsumoto K 2019 *Front. Phys.* **7** 82

[5] Vulusala G V S and Madichetty S 2018 *Int. J. Energy Res.* **42** 358

[6] Macmanus-Driscoll J L and Wimbush S C 2021 *Nat. Rev. Mater.* **6** 587

[7] Obradors X and Puig T 2014 *Supercond. Sci. Technol.* **27** 044003

[8] Kwok W K, Welp U, Glatz A, Koshelev A E, Kihlstrom K J and Crabtree G W 2016 *Rep. Prog. Phys.* **79** 116501

[9] Larbalestier D, Gurevich A, Feldmann D M and Polyanskii A 2001 *Nature* **414** 368

[10] Rijckaert H, Pollefeyt G, Sieger M, Hänisch J, Bennewitz J, De Keukeleere K, De Roo J, Hühne R, Bäcker M, Paturi P, Huhtinen H, Hemgesberg M and Van Driessche I 2017 *Chem. Mater.* **29** 6104

[11] Díez-Sierra J, López-Domínguez P, Rijckaert H, Rikel M, Hänisch J, Khan M Z, Falter M, Bennewitz J, Huhtinen H, Schäfer S, Müller R, Schunk S A, Paturi P, Bäcker M, De Buysser K and Van Driessche I 2020 *ACS Appl. Nano Mater.* **3** 5542

[12] Huang R T, Chen J, Liu Z Y, Wang G and Cai C B 2024 *Adv. Funct. Mater.* **34** 2401251

[13] Huang R T, Chen J, Liu Z Y, Dou W Z, Zhang N and Cai C B 2023 *Supercond. Sci. Technol.* **36** 125002

[14] Fujiwara H 2007 *Spectroscopic Ellipsometry: Principles and Applications* (Chichester: John Wiley & Sons)

[15] Wee A T, Yin X M and Tang C S 2022 *Introduction to Spectroscopic Ellipsometry of Thin Film Materials: Instrumentation, Data Analysis and Applications* (Chichester: John Wiley & Sons)

[16] Sun M X, He X, Chen M Y, Tang C S, Liu X F, Dai L, Liu J S, Zeng Z G, Sun S, Breese M B H, Cai C B, Wang L, Du Y G, Wee A T S and Yin X M 2024 *ACS Photonics* **11** 2324

[17] Fan F, Lu Y M, Liu Z Y, Zhou D F, Guo Y Q, Bai C Y, Li M J and Cai C B 2020 *Supercond. Sci. Technol.* **33** 055003

[18] Holesinger T G, Civale L, Maiorov B, Feldmann D M, Coulter J Y, Miller D J, Maroni V A, Chen Z, Larbalestier D C, Feenstra R, Li X, Huang Y, Kodenkandath T, Zhang W, Rupich M W and Malozemoff A P 2008 *Adv. Mater.* **20** 391

[19] Qi X and Macmanus-Driscoll J L 2001 *Curr. Opin. Solid State Mater. Sci.* **5** 291

[20] Kim B J, Chung S and Cho S M 2002 *Applied Surface Science* **187** 124

[21] Wang Y, Zhao S C, Zeng Z G, Jia Z Y, Xiao S L, Wu K R and Cai C B 2023 *J. Low Temp. Phys.* **210** 484

[22] Sun Z Y, Wang S S, Wu K, Liu Q and Han Z 2004 *Physica C* **412** 1331

[23] Zeng L, Lu Y M, Liu Z Y, Chen C Z, Gao B and Cai C B 2012 *J. Appl. Phys.* **112** 053903

[24] Hong S, Cheong H and Park G 2010 *Physica C* **470** 383

[25] Wang S S, Gu B F, Li F, Wu H, Muhammad S, Dahal Y P, Xiao Z S and Ouyang X P 2021 *J. Alloys Compd.* **863** 158607

[26] Hebard A F, Fleming R M, Short K T, White A E, Rice C E, Levi A F J and Eick R H 1989 *Appl. Phys. Lett.* **55** 1915

[27] Bozovic I 1990 *Phys. Rev. B* **42** 1969

[28] Cooper S L, Reznik D, Kotz A, Karlow M A, Liu R, Klein M V, Lee W C, Giapintzakis J, Ginsberg D M, Veal B W and Paulikas A P 1993 *Phys. Rev. B* **47** 8233

[29] Molina-Luna L, Duerrschnabel M, Turner S, Erbe M, Martinez G T, Van Aert S, Holzapfel B and Van Tendeloo G 2015 *Supercond. Sci. Technol.* **28** 115009

[30] Garriga M, Humlíček J, Barth J, Johnson R L and Cardona M 1989 *J. Opt. Soc. Am. B* **6** 470

[31] Arima T, Kikuchi K, Kasuya M, Koshihara S, Tokura Y, Ido T and Uchida S 1991 *Phys. Rev. B* **44** 917

[32] Kelly M K, Barboux P, Tarascon J M and Aspnes D E 1989 *Phys. Rev. B* **40** 6797

[33] Asmara T C, Wan D Y, Zhao Y L, Majidi M A, Nelson C T, Scott M C, Cai Y, Yan B X, Schmidt D, Yang M, Zhu T, Trevisanutto P E, Motapothula M R, Feng Y P, Breese M B H, Sherburne M, Asta M, Minor A, Venkatesan T and Rusydi A 2017 *Nat. Commun.* **8** 15271